RSC Advances

PAPER

View Article Online
View Journal | View Issue

Cite this: *RSC Adv.*, 2017, **7**, 28069

Direct synthesis and characterization of mixed-valent $Li_{0.5-\delta}CoPO_4$, a Li-deficient derivative of the *Cmcm* polymorph of $LiCoPO_4$†

Jennifer Ludwig,[a] Carlos Alarcón-Suesca,[a] Stephan Geprägs,[b] Dennis Nordlund,[c] Marca M. Doeff,[d] Inés Puente Orench[ef] and Tom Nilges*[a]

While the majority of research activities on $LiCoPO_4$ is focussed on the thermodynamically stable olivine-type *Pnma* polymorph, the metastable $Pna2_1$ and *Cmcm* modifications have recently attracted considerable attention due to their interesting material properties. In this study, we present the first Li-deficient structural derivative of the *Cmcm* modification with the nominal composition $Li_{0.5-\delta}CoPO_4$. As opposed to the substoichiometric olivine (*Pnma*) phases Li_xCoPO_4 (x = 0; 2/3), which are exclusively accessible by electrochemical or chemical Li extraction techniques, this is also the first time that a direct soft-chemical synthesis route towards a Li_xCoPO_4-type material is accomplished. X-ray and neutron diffraction studies indicate that *Cmcm*-type $Li_{0.5-\delta}CoPO_4$ shows vacancies on both the Li and Co sites, whereas X-ray absorption spectra demonstrate that the structure features heterovalent Co ions (+2/+3) to compensate for the Li deficit. Magnetic measurements reveal a long-range antiferromagnetic order below 10.5 K. A thorough investigation of the thermal stability using thermogravimetric analysis, differential scanning calorimetry, and temperature-dependent *in situ* X-ray powder diffraction demonstrates that $Li_{0.5-\delta}CoPO_4$ is metastable and exhibits a complex, multi-step thermal decomposition mechanism. In the first step at 394 °C, it decomposes to α-$Co_2P_2O_7$ ($P2_1/c$) and $LiCoPO_4$ (*Cmcm*) upon O_2 release. The $LiCoPO_4$ (*Cmcm*) intermediate is then irreversibly transformed to olivine-type $LiCoPO_4$ (*Pnma*) at 686 °C. The material properties of $Li_{0.5-\delta}CoPO_4$ are further compared to the fully lithiated, isostructural $LiCoPO_4$ (*Cmcm*) phase, for which an improved structure solution as well as Co $L_{2,3}$-edge X-ray absorption spectra are reported for the first time.

Received 9th April 2017
Accepted 14th May 2017

DOI: 10.1039/c7ra04043a

rsc.li/rsc-advances

Introduction

In the last two decades, thermodynamically stable, olivine-type (space group: *Pnma*) $LiCoPO_4$ polymorphs have been extensively studied as a high-voltage cathode material for lithium-ion batteries (operating voltage: ~4.8 V *vs.* Li/Li^+; theoretical capacity: 167 mA h g^{-1}).[1–4] The three-dimensional network structure features $[CoO_6]$ octahedra, $[PO_4]$ tetrahedra, and Li^+ ions in octahedral voids.[5] The majority of research activities have been focused on optimizing the electrochemical performance of the material.[4,6,7] However, despite intensive efforts, the nature of the intermediate phase Li_xCoPO_4, which occurs upon the two-step Li insertion–extraction reaction of $LiCoPO_4$,[8] is still under investigation and debated in the literature. Earlier

[a]*Technical University of Munich, Department of Chemistry, Synthesis and Characterization of Innovative Materials, Lichtenbergstr. 4, 85747 Garching, Germany. E-mail: tom.nilges@lrz.tum.de*

[b]*Walther Meissner Institute, Bavarian Academy of Sciences and Humanities, Walther-Meissner-Str. 8, 85747 Garching, Germany*

[c]*Stanford Synchrotron Radiation Lightsource, SLAC National Accelerator Laboratory, 2575 Sand Hill Rd, Menlo Park, CA, 94025, USA*

[d]*Lawrence Berkeley National Laboratory, Energy Storage and Distributed Resources Division, 1 Cyclotron Rd, Berkeley, CA, 94720, USA*

[e]*Instituto de Ciencia de Materiales de Aragón, Pedro Cerbuna 12, 50009 Zaragoza, Spain*

[f]*Institut Laue-Langevin, 71 Avenue des Martyrs, B.P. 156, 38042 Grenoble Cedex 9, France*

† Electronic supplementary information (ESI) available: (1) Comparison of the PXRD patterns of $Li_{0.5-\delta}CoPO_4$ and $Li_{1-\gamma}CoPO_4$, (2) Rietveld refinement details from PXRD data, (3) Rietveld refinement details from neutron powder diffraction data, (4) additional illustrations of the crystal structure, (5) electrochemical characterization, (6) SEM and EDS analysis, (7) full IR spectra, (8) additional magnetic data, (9) Rietveld refinement details of the PXRD pattern of the sample obtained from the TGA/DSC measurement of $Li_{0.5-\delta}CoPO_4$ under air, (10) thermal stability under Ar (TGA/DSC, Rietveld refinement), (11) Rietveld fits and crystallographic data of the *in situ* PXRD patterns (30–700 °C; air), (12) additional *in situ* PXRD patterns (800 °C, 900 °C, and 25 °C; air). The cif files containing the crystallographic data of $Li_{0.5-\delta}CoPO_4$ and $Li_{1-\gamma}CoPO_4$ can be obtained from FIZ Karlsruhe, 76344 Eggenstein-Leopoldshafen, Germany (fax: +49 7247 808 666; e-mail: crysdata@fiz-karlsruhe.de), on quoting the CSD deposition numbers 432850 and 432851. For ESI and crystallographic data in CIF or other electronic format see DOI: 10.1039/c7ra04043a

investigations suggested compositions of $Li_{0.7}CoPO_4$ (ref. 8) and $Li_{0.6}CoPO_4$,[9] respectively, whereas a later report[10] stated a Li_xCoPO_4 ($x = 0.20$–0.45) composition. Recently, the lithiation state of the intermediate was determined to be $Li_{2/3}CoPO_4$ by two independent studies.[11,12] Since the completely delithiated phase $CoPO_4$ is unstable and undergoes amorphization when exposed to air or moisture,[8,9] the application of inert gas atmospheres and/or *in situ* techniques is crucial. According to Bramnik *et al.*,[13] both lithium-poor, Co^{3+}-containing phases are intrinsically instable and exhibit a low thermal stability. Charged $LiCoPO_4$ electrodes were shown to decompose rapidly at temperatures below 200 °C, leading to gas evolution and the crystallization of $LiCoPO_4$ (only in the case of Li_xCoPO_4) and $Co_2P_2O_7$. In contrast, Theil *et al.*[14] claimed that Li_xCoPO_4 is thermally stable up to 550 °C and that the thermal instability of charged $LiCoPO_4$ electrodes can be solely ascribed to the instability of the $CoPO_4$ phase. To the best of our knowledge, these Li-deficient phases are exclusively accessible by electrochemical or chemical Li extraction from $LiCoPO_4$ (*Pnma*),[9,13] and a direct synthesis route has not been reported to date. Interestingly, in contrast to previous reports,[15,16] we recently demonstrated[17] that also the fully lithiated olivine-type $LiCoPO_4$ does not exhibit unlimited thermal stability since it transforms to the (at room temperature) metastable *Pna*2_1-$LiCoPO_4$ phase around 900 °C.

The less common, metastable $LiCoPO_4$ modifications, which crystallize in the space groups *Pna*2_1 (ref. 16, 18 and 19) and *Cmcm*, (ref. 16, 20 and 21) have recently attracted attention because of their interesting material properties and potential applicability as cathode materials for Li-ion batteries. The *Pna*2_1 modification exhibits a network of $[PO_4]$ and $[CoO_4]$ tetrahedra and Li^+ ions on tetrahedral sites.[18] To date, the polymorph has only been accessible by microwave-assisted synthesis techniques.[16,18,19] *Pna*2_1-type $LiCoPO_4$ shows the highest redox potential of ~5.0 V *vs.* Li/Li^+ compared to the other two $LiCoPO_4$ polymorphs.[16,18] A single redox peak was observed upon cycling, indicating that the compound is delithiated in one step. However, the electrochemical performance was found to be poor (maximum capacity: 33 mA h g^{-1}).[16,18,19] Magnetic measurements indicated a paramagnetic Curie–Weiss-like behavior at high temperatures, and a long-range antiferromagnetic order below $T_N = 11$ K.[18] Recently, a structure redetermination suggested that the material is non-stoichiometric and shows Li–Co anti-site defects, which provide an explanation for this poor performance.[19] A thorough investigation of the thermal stability revealed that $LiCoPO_4$ (*Pna*2_1) converts to the olivine $LiCoPO_4$ (*Pnma*) modification at 527 °C.[19] Interestingly, the *Pna*2_1 structure re-emerges as a stable high-temperature phase above 800 °C.[19]

The $LiCoPO_4$ (*Cmcm*) polymorph was first reported by Amador *et al.*[20] using a high-pressure, high-temperature synthesis route (6 GPa, 900 °C). Alternative pathways using low-temperature procedures such as microwave-assisted solvothermal[16] and polyol[21] synthesis have been demonstrated recently. The structure is built from $[CoO_6]$ and $[PO_4]$ units, with Li^+ ions occupying tetrahedral sites. $LiCoPO_4$ (*Cmcm*) shows a single redox peak at ~4.3 V *vs.* Li/Li^+ upon cycling,[16] which corresponds to the lowest redox potential of all the $LiCoPO_4$ polymorphs. A discharge capacity of only 6 mA h g^{-1} has been reported, which was associated with the poor conductivity of the material.[16] The magnetic characterization suggested a long-range antiferromagnetic order below $T_N = 11$ K at low fields (10 kOe) and the presence of a metamagnetic transition.[21] Investigations on the thermal stability showed that the structure is metastable and transforms to olivine-type $LiCoPO_4$ (*Pnma*) at 575 °C, which then transforms to the *Pna*2_1 modification at 675 °C. The thermodynamically stable *Pnma*-$LiCoPO_4$ phase was obtained after cooling.[21]

Based on our previous work on the three $LiCoPO_4$ polymorphs,[17,19,21] we herein present the first Li-deficient structural derivative of the *Cmcm* modification with the nominal composition $Li_{0.5-\delta}CoPO_4$. To the best of our knowledge, this is the first time that a sub-stoichiometric Li_xCoPO_4 phase has been synthesized directly (bottom-up) by a soft-chemical polyol approach as opposed to electrochemical or electrochemical Li extraction (top-down) techniques described in the literature.[9,13] The structure, morphology, oxidation state as well as electrochemical and magnetic properties of the novel *Cmcm*-type phase $Li_{0.5-\delta}CoPO_4$ are investigated. Moreover, the thermal properties are studied using thermogravimetry, differential scanning calorimetry, and temperature-dependent *in situ* X-ray powder diffraction. The results are discussed in context of the 'fully lithiated' $LiCoPO_4$ (*Cmcm*) phase, for which an improved structure solution (revealing a sub-stoichiometry reflected by the revised empirical formula $Li_{1-\gamma}CoPO_4$) as well as X-ray absorption spectra are presented for the first time.

Experimental

Synthesis of $Li_{0.5-\delta}CoPO_4$ (*Cmcm*) and $Li_{1-\gamma}CoPO_4$ (*Cmcm*)

Cmcm-type $LiCoPO_4$ samples with varied Li contents were obtained from a polyol process as described in our previous work[21] using $LiCH_3COO$ (ChemPur, 99+%), $(Co(CH_3COO)_2 \cdot 4H_2O$, Merck, 99.99%), and H_3PO_4 (Merck, 85 wt%) as precursors, and tetraethylene glycol (TTEG, Merck, ≥99.0%) as solvent. For the synthesis of $Li_{1-\gamma}CoPO_4$ (*Cmcm*), a Li : Co : P molar ratio of 3 : 1 : 10 was used, whereas $Li_{0.5-\delta}CoPO_4$ (*Cmcm*) was obtained from a modified process using a ratio of 1 : 1 : 10. First, H_3PO_4 was added dropwise to a solution of cobalt acetate in 125 mL TTEG. Then, a second solution containing lithium acetate in 75 mL TTEG was added. The resulting mixture was refluxed at 185 °C for 14 h in a round-bottom flask. After cooling, the precipitate was recovered by centrifugation (1500 rpm, 20 min, three times) and washed with ethanol (VWR AnalaR NORMAPUR, 99.95%). The light pink powder (*cf.* graphical abstract) was collected by filtration, washed with acetone (99%), and dried in air at 100 °C for 14 h. Note that in contrast to the delithiated *Pnma* structures Li_xCoPO_4 and in particular $CoPO_4$, which are sensitive to air and moisture,[8,9] the *Cmcm*-derivative $Li_{0.5-\delta}CoPO_4$ is stable under air for at least several months.

X-ray powder diffraction (PXRD) and Rietveld refinement details

Room-temperature PXRD data of the ground powders sealed in borosilicate glass capillaries (0.5 mm, Hilgenberg) were

collected on a Stoe STADI P diffractometer (Mo $K_{\alpha1}$ radiation, λ = 0.70930 Å; Ge(111) monochromator; Dectris MYTHEN DCS 1K silicon solid-state detector) in a 2θ range of 3–60° (PSD step: 0.015°; time per step: 30 s, three ranges, total measurement time: 12 h). The diffraction patterns were calibrated using an external silicon standard. The Jana2006 software[22] was used for the structure refinement by the Rietveld method, using the recently reported structure solution of $LiCoPO_4$ (*Cmcm*; ICSD no. 432186)[21] as a starting model. Details on the Rietveld refinement strategy and parameters used can be found in our previous work.[21]

Neutron powder diffraction (NPD) experiments

Neutron powder diffraction data were collected using the diffractometer D2B at the Institut Laue-Langevin (ILL, Grenoble, France), working at a calibrated wavelength of 1.5942 Å in a 2θ range of 5–160°. The data were recorded at 296 K with a collection time of 4 h per pattern. The data were analyzed by the Rietveld method with the FULLPROF program.[23] The line shape of the diffraction peaks was generated by a pseudo-Voigt function. The instrumental contribution to the peak broadening was determined using an instrument resolution function built from the refinement of a $Na_2Ca_3Al_2F_{14}$ standard, while the wavelength was refined using a Si standard.

Elemental analysis

Analysis of the Li, Co, and P contents was carried out by atomic absorption spectroscopy (AAS, Varian AA280FS sequential device) and photometry (Shimadzu UV-160 photometer). A Hekatech Euro EA CHNSO combustion analyzer was used to determine the C, H, N, and S amounts.

Soft X-ray absorption spectroscopy (soft XAS)

Co $L_{2,3}$-edge soft XAS spectra were collected at beamline 8–2 of Stanford Synchrotron Radiation Lightsource (SSRL), operating the spherical grating monochromator (SGM, ruling: 1100 mm^{-1}) with 40 × 40 μm slits (resolution: ~0.3 eV), as described in our previous work.[17] The XAS spectra presented in this report are derived from the total electron yield (TEY), measured *via* the drain current (probing depth: 2–5 nm). We also recorded Auger electron yield (AEY) and total fluorescence yield (FY) spectra *via* a cylindrical mirror analyzer and a silicon diode (AXUV100). These modes, which probe ~2 nm and 50–100 nm deep, respectively, ensured that the best quality TEY spectra was bulk representative and that the contribution from surface contamination was small. All spectra were normalized to the incoming flux and the energy scale was calibrated to match that of ref. 24, followed by a background subtraction to a line, and a final area normalization for comparison. In order to produce the most stable and reproducible fits, the fitting was limited to the region just around the L_3 edge (774–784 eV), in which the normalization was further restricted through another line subtraction and area normalization.

Fourier-transform infrared (FTIR) spectroscopy

IR spectra were collected on a Varian 670 FTIR spectrometer equipped with a PIKE GladiATR diamond ATR stage. The measurements were performed using 132 scans in a wavenumber range of 400–4000 cm^{-1}.

Magnetic measurements

DC magnetization measurements were performed using a Quantum Design MPMS XL7 SQUID magnetometer in the temperature range from 2 K to 300 K with a magnetic field of up to 7 T. The powder samples were placed inside gelatin capsules. The temperature-dependent magnetic moments were recorded under an applied magnetic field of 1 kOe after cooling the samples under a magnetic field of 7 T (field-cooled, FC) and 0 T (zero field-cooled, ZFC). Magnetic hysteresis measurements were carried out with magnetic field strengths between −7 T and 7 T at 2 K, 11 K, and 300 K, respectively.

Thermogravimetric analysis (TGA) and differential scanning calorimetry (DSC)

The stability of the material (specimen weight: ~10 mg) upon heating was assessed using a simultaneous Mettler Toledo TGA/DSC 1 STAR device, which did not allow to monitor the cooling cycle due to the setup. The measurement was run in a temperature range of 30–900 °C (heating rate: 10 °C min^{-1}) in an argon stream (10 mL min^{-1}), and additionally synthetic air (10 mL min^{-1}) in order to ensure comparability of the data with the *in situ* PXRD experiment.

Temperature-dependent *in situ* X-ray powder diffraction (PXRD)

Temperature-controlled PXRD was performed *in situ* under air using a PANalytical X'Pert Pro diffractometer (Bragg–Brentano geometry; Cu K_α radiation; XCelerator detector) equipped with an Anton Parr HTK-1200 hot stage and a TCU 1000N temperature controller. The material was placed inside a corundum flat plate sample holder and heated up to 900 °C in steps of 100 °C (heating rate: 5 °C min^{-1}), with each temperature being held for 5 min before collecting the data. The scans were recorded in a 2θ range of 15–70° (step: 0.022°; time per step: 209.5 s; total experiment time: 145.5 h).

Results and discussion

Rietveld refinement of X-ray and neutron powder diffraction data

Fig. 1a shows the Rietveld fit of the X-ray powder diffraction pattern of the as-prepared title compound $Li_{0.5-\delta}CoPO_4$. The pattern of a reproduced sample of *Cmcm*-type $LiCoPO_4$ (Fig. 1b) is in good agreement with our previous work.[21] In both cases, all the reflections can be indexed in the orthorhombic space group *Cmcm* and no additional reflections are observed, indicating that both materials are phase pure. While the pattern of $Li_{0.5-\delta}CoPO_4$ appears to be roughly similar to the one of $LiCoPO_4$, suggesting that the crystal structure of the Li-deficient

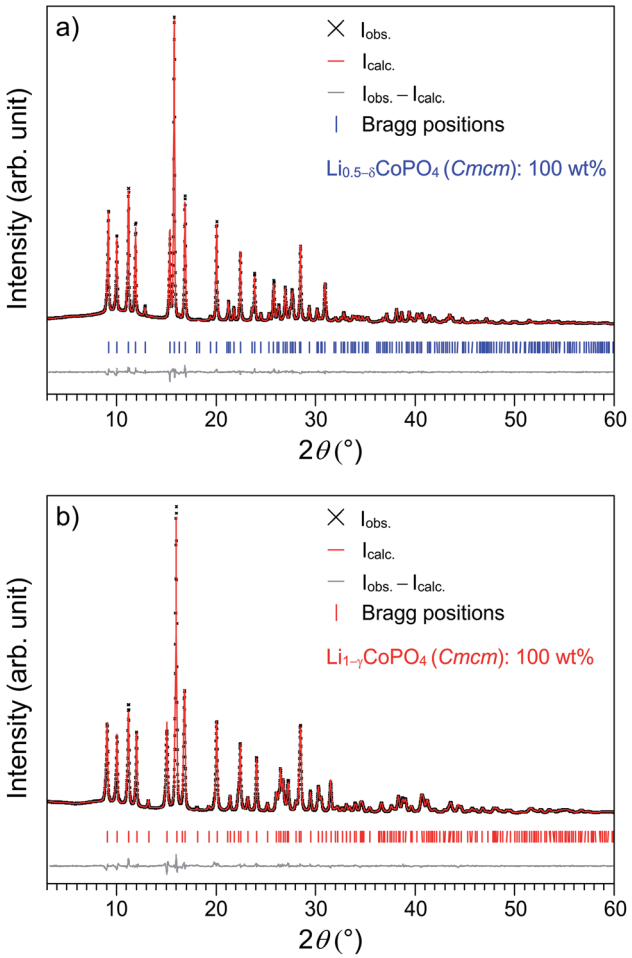

Fig. 1 Rietveld fits of the X-ray powder diffraction data (transmission geometry, Mo $K_{\alpha 1}$ radiation) of (a) $Li_{0.5-\delta}CoPO_4$ (*Cmcm*; refined composition: $Li_{0.39(2)}Co_{0.96(1)}PO_4$, $\delta = 0.11(2)$), and (b) $Li_{1-\gamma}CoPO_4$ (*Cmcm*, refined composition: $Li_{0.94(2)}Co_{0.96(1)}PO_4$, $\gamma = 0.06(2)$).

compound is strongly correlated with the one of the fully lithiated material, some shifts in the peak positions can be recognized. The most significant feature of the $Li_{0.5-\delta}CoPO_4$ pattern is the narrowing of the (200) and (112) reflections at 15.0° and 15.9° 2θ. Furthermore, a completely different peak pattern can be observed in the 2θ region of 25.5–27.5° (for a detailed view, please refer to Fig. S1, ESI†).

To gain further insights into the structural differences causing the peak shifts, a Rietveld refinement was performed, using the previously published structure solution of *Cmcm*-type $LiCoPO_4$ (ICSD no. 143186)[21] as a starting model. Since the elemental analysis indicated an approximate 50% deficit in Li for $Li_{0.5-\delta}CoPO_4$ compared to *Cmcm*-$LiCoPO_4$ (*cf.* Table 2) within standard deviations, the structures were at first refined with fixed Li site occupancy factors of 50% and 100%, respectively, resulting in good reliability factors (Table S1, ESI†). Taking into account that the empirical formulas derived from elemental analysis indicated a deficit in both Li and Co for the two materials (empirical formulas: $Li_{0.45(5)}Co_{0.93(3)}P_{1.00(2)}O_4$ and $Li_{0.93(5)}Co_{0.91(3)}P_{1.00(2)}O_4$; *cf.* Table 2), we tentatively refined the occupancy factors of the Li and Co sites after having applied an absorption correction.[25] In both cases, the free refinement resulted in statistically significant values for the occupancies (39(2)% Li and 96.4(5)% Co for $Li_{0.5-\delta}CoPO_4$; $\delta = 0.11(2)$ and 94(2)% Li and 95.5(5)% Co for $LiCoPO_4$, *cf.* Table S2, ESI†), indicating that both structures feature vacancies in the cationic substructures and are non-stoichiometric. In both cases, the reliability factors were significantly improved over the previous structure models with fixed occupancies (*cf.* Tables 1 and S1, ESI†). To simplify the sum formulas of both compounds while still reflecting the off-stoichiometry from the idealized formulas $Li_{0.5}CoPO_4$ and $LiCoPO_4$ (within three standard deviations), the compounds are referred to as $Li_{0.5-\delta}CoPO_4$ for the Li-deficient phase, and $Li_{1-\gamma}CoPO_4$ (with $\gamma = 0.06(2)$) for *Cmcm*-type $LiCoPO_4$ in this work. It is worth noting that on basis of these refinements, there was no indication for the occurrence of anti-site defects, which are profound for materials synthesized at low temperatures (as observed *e.g.* in $Pna2_1$-type $LiCoPO_4$).[19] Furthermore, in contrast to $Li_{0.94(2)}Co_{0.96(1)}PO_4$, the composition of the Li-deficient *Cmcm* derivative $Li_{0.39(2)}Co_{0.96(1)}PO_4$ would not be charge-balanced assuming that Co is only present in the oxidation state +2. We therefore assume that the deficit in positive electric charge caused by the lower Li^+ content is compensated by Co^{3+} in the framework, which was confirmed by X-ray absorption spectroscopic studies discussed later.

The refined cell parameters (Table 1) indicate a significant contraction along the *a* axis and an expansion along the *c* axis for $Li_{0.5-\delta}CoPO_4$ compared to $Li_{1-\gamma}CoPO_4$, while *b* is not significantly changed, hence providing an explanation for the peak shifts observed in the PXRD patterns. Furthermore, the respective cell volumes ($V = 278.116(19)$ Å^3 *vs.* 276.28(2) Å^3, corresponding to an increase of 0.7%) reveal that the $Li_{0.5-\delta}CoPO_4$ structure is less dense, which is consistent with the decrease in crystal densities. This is surprising since for the delithiated phases Li_xCoPO_4 and $CoPO_4$ derived from olivine-

Table 1 Crystallographic parameters of (a) $Li_{0.5-\delta}CoPO_4$ in comparison with (b) $Li_{1-\gamma}CoPO_4$ (both *Cmcm*, $Z = 4$) as refined from X-ray powder diffraction data ($T = 298$ K)[a]

Sample	(a) $Li_{0.5-\delta}CoPO_4$	(b) $Li_{1-\gamma}CoPO_4$
Empirical formula	$Li_{0.39(2)}Co_{0.96(1)}PO_4$	$Li_{0.94(2)}Co_{0.96(1)}PO_4$
M_r (g mol^{-1})	154.3	158.1
Crystal system	Orthorhombic	Orthorhombic
Space group (no.)	*Cmcm* (63)	*Cmcm* (63)
Z	4	4
a (Å)	5.3385(2)	5.4432(3)
b (Å)	8.1763(3)	8.1695(4)
c (Å)	6.3716(2)	6.2128(3)
V (Å^3)	278.116(19)	276.28(2)
$F(000)$	297	302
ρ (calcd) (g cm^{-3})	3.684(1)	3.800(1)
R_p	0.0257	0.0196
R_{wp}	0.0327	0.0255
R_{exp}	0.0267	0.0252
R_F	0.0143	0.0106
R_B	0.0254	0.0184
χ^2	1.23	1.01
Data/restraints/parameter	3800/0/59	3835/0/57

[a] The estimated standard deviations were calculated by the Berar's procedure and are indicated in parentheses.

type $LiCoPO_4$ (*Pnma*), a significant decrease in cell volume of up to ~7% ($CoPO_4$) was observed due to the smaller ionic radius of Co^{3+} compared to Co^{2+}.[8,9,11] The slight increase in cell volume might be explained by the fact that our Li-poor *Cmcm* material was produced from a kinetically controlled synthesis as opposed to *Pnma*-type $CoPO_4$, which was obtained by electrochemical Li extraction. As a result, the Li ions and voids are likely to be statistically distributed within the *Cmcm* structure. This would also be in line with investigations on olivine-type $LiFePO_4$, which revealed that materials synthesized at low temperature are prone to disorder, resulting in larger cell volumes than expected.[26] However, a thorough investigation of the Li^+/vacancy distributions in the structures is beyond this work.

In order to further verify the Li contents and the structure model, we performed additional neutron powder diffraction (NPD) studies of both samples. Rietveld refinements of the NPD data were carried out using the structure parameters obtained from the PXRD experiment as a starting model. Then, the atomic coordinates, thermal parameters as well as occupation factors of Li and Co were refined (see Fig. S2 (ESI†) for the Rietveld fits). The refined lattice parameters (Table S4, ESI†) are in good agreement with the X-ray data. The refinement of the site occupancy factors revealed 37(4)% Li and 98(2)% Co for $Li_{0.5-\delta}CoPO_4$ ($\delta = 0.13(4)$), and 90(3)% Li and 95(6)% Co for $Li_{1-\gamma}CoPO_4$ ($\gamma = 0.10(3)$) (Table S5, ESI†). The compositions and structural parameters of $Li_{0.37(4)}Co_{0.98(1)}PO_4$ and $Li_{0.90(2)}Co_{0.95(6)}PO_4$ are very close to the ones derived from the X-ray experiment and hence confirm the structure model.

Crystal structure

The structures of both *Cmcm*-type $LiCoPO_4$ materials feature rows of edge-sharing, distorted $[CoO_6]$ octahedra which are running along the [001] direction as illustrated in Fig. 2a.[20,27] The $[CoO_6]_\infty$ rows are cross-linked along [100] by alternating pairs of edge-sharing, asymmetric $[PO_4]$ and $[LiO_4]$ units (note that the tetrahedrally coordinated Li ions are shown in Fig. 2 instead of $[LiO_4]$ tetrahedra for clarity). As a result, layers of the composition $([CoO_6][LiO_4][PO_4])_\infty$ are formed in the *ac* plane (Fig. 2b). In these layers, every $[CoO_6]$ octahedron shares two opposite O2–O2 edges with neighboring $[CoO_6]$ units, and two apical O2 atoms with two different $[PO_4]$ and $[LiO_4]$ tetrahedra, which connect the $[CoO_6]_\infty$ strands (for details see Fig. S3, ESI†). The layers are in turn stacked in the sequence AB (indicated by black and grey boxes in Fig. 2a and c) along [010] with a displacement of *a*/2 *via* the apical O1 atoms of the $[CoO_6]$ units so that a three-dimensional framework is formed. It has to be emphasized that despite the fact that Li channels seem to occur along [100] (Fig. 2a), the Li–Li distances are very large (d = 5.3385(4) Å and 5.4432(5) Å, *cf.* Table S3b and d, ESI†), so that these sites are considered isolated. Hence, Li migration will require a very high activation energy along this path and the Li mobility is extremely low in both structures.[20,27] The lack of suitable Li migration pathways is confirmed by electrochemical measurements (see Section 5 and Fig. S4, ESI†) that revealed a very poor performance for both *Cmcm* materials (discharge capacities of < 3 mA h g^{-1}), and is also in line with a previous report.[16] Hence, due to the intrinsically low Li-ion conductivity, the $Li_{0.5-\delta}CoPO_4$ and $Li_{1-\gamma}CoPO_4$ phases cannot be considered suitable for battery applications.

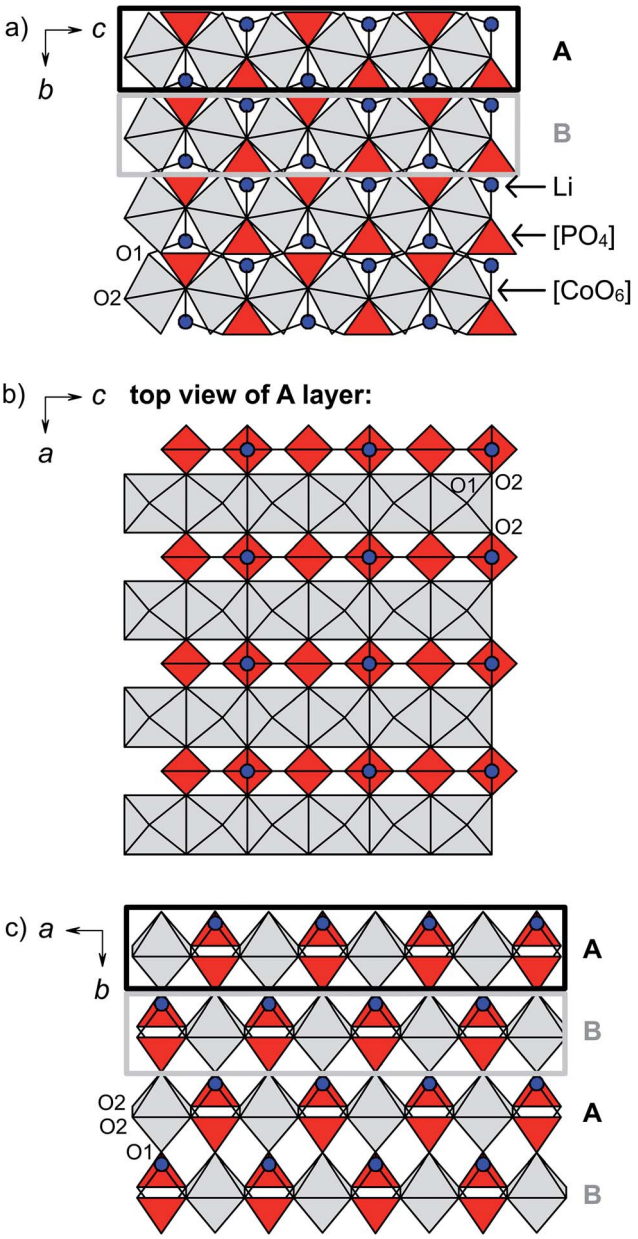

Fig. 2 Polyhedral illustration of the crystal structures of *Cmcm*-type $Li_{0.5-\delta}CoPO_4$ and $Li_{1-\gamma}CoPO_4$ viewed along (a) [100], (b) [010] (showing one A layer as indicated by the black boxes in a, c), and (c) [001]. $[CoO_6]$ octahedra are displayed in grey, $[PO_4]$ tetrahedra in red, and tetrahedrally coordinated Li ions in blue (for clarity, no T_d representation was used for the $[LiO_4]$ units). The structure is built from $([CoO_6][LiO_4][PO_4])_\infty$ layers in the *ac* plane (b), which are stacked along *b* in the sequence AB (c). The layers consist of rows of edge-sharing $[CoO_6]$ octahedra (a), which are connected by alternating pairs of $[LiO_4]$ and $[PO_4]$ units. The occupancies on the Li and Co sites are 39(2)% Li and 96.5(5)% Co for $Li_{0.5-\delta}CoPO_4$, and 94(2)% Li and 95.5(5)% Co for $Li_{1-\gamma}CoPO_4$.

The structural differences between $Li_{1-\gamma}CoPO_4$ and its Li-deficient analogue $Li_{0.5-\delta}CoPO_4$ can be derived from the cell parameters (Table 1) and the interatomic distances (Table S3b and d, ESI†). In general, the framework of $Li_{0.5-\delta}CoPO_4$ is contracted by ~0.10 Å in the *a* dimension and expanded by ~0.16 Å and ~0.01 Å along *c* and *b*, respectively, as also indicated by the distances between the Co centers in and between the layers. The average Co–O (2.122 Å in $Li_{0.5-\delta}CoPO_4$ *vs.* 2.123 Å in $LiCoPO_4$) and P–O (1.539 Å *vs.* 1.538 Å) distances in the $[CoO_6]$ and $[PO_4]$ units remain virtually unchanged, which is surprising since one would expect a decrease in the Co–O distances due to the occurrence of a definite amount of the smaller Co^{3+} ion compared to Co^{2+} in the structure. The individual bond lengths, however, reveal that both the $[CoO_6]$ and $[PO_4]$ units show a higher degree of distortion. This is reflected by the fact that the Co–O2 and P–O2 distances (in the $([CoO_6][LiO_4][PO_4])_\infty$ layers) are shortened, whereas the Co–O1 and P–O1 bonds (connecting the layers along *b*) are expanded, resulting in an increase of the distance between the A–B layers (*cf.* Co–P distances). On the other hand, the mean Li–O distances are increased by ~0.4 Å, leading to an expansion of the "channels" along [100]. This is consistent with the increase of the Li–Li distances by ~0.10 Å. However, it has to be noted that we cannot provide any information about the ordering of the Li^+, Co^{2+}, and Co^{3+} ions or the vacancies in the structure. Based on considerations on the charge distribution, it is likely that the vacancies in the $Li_{0.5-\delta}CoPO_4$ framework are located next to the Co^{3+} centers, which would be consistent with DFT (density functional theory) studies[12] on the Li^+/vacancy distribution in olivine-type $Li_{2/3}CoPO_4$.

Elemental analysis

The results of the elemental analysis of $Li_{0.5-\delta}CoPO_4$ (*Cmcm*) are compared to the values of *Cmcm*-type $LiCoPO_4$ from our recent report[21] in Table 2. The CHNS analyses are similar and show small amounts of hydrogen and carbon in both materials, which arise from residual tetraethylene glycol (TTEG) solvent or the decomposition products of TTEG and the acetate precursors. Whereas the Co and P contents (in wt%) are comparable within three standard deviations, it is evident that the novel compound contains about half the amount of Li (2.0(2) wt%) compared to the $LiCoPO_4$ (*Cmcm*) material (4.1(2) wt%). This is confirmed by the respective Li : Co : P molar ratios of 0.45(5):0.93(3):1.00(2) and 0.93(5):0.91(5):1.00(2). EDS measurements further substantiate the Co : P ratios found by elemental analyses. (Images of the obtained crystal morphologies and semi-quantitative EDS analyses are provided in Fig. S5, ESI†.) The empirical sum formulas derived from elemental analysis, $Li_{0.45(5)}Co_{0.93(3)}P_{1.00(2)}O_4$ and $Li_{0.93(5)}Co_{0.91(3)}P_{1.00(2)}O_4$, indicate a deficit both in Li and Co for both compounds and are also consistent with the results of the Rietveld refinements (*cf.* Table 1) within standard deviations. Based on the results of the elemental analysis, δ in this case is 0.05(5) in $Li_{0.5-\delta}CoPO_4$ (whereas γ is 0.07(5) in $Li_{1-\gamma}CoPO_4$), which is slightly smaller than derived from X-ray and neutron diffraction. Due to the kinetically controlled synthesis procedure, however, it is possible that the composition will slightly vary from batch to batch. Summarizing all efforts from diffraction experiments and elemental analysis to determine the Li and Co contents of the present phases, the notations $Li_{0.5-\delta}CoPO_4$ and $Li_{1-\gamma}CoPO_4$ seem therefore to best reflect the off-stoichiometries found by the different techniques within three standard deviations.

Table 2 Elemental analysis of (a) $Li_{0.5-\delta}CoPO_4$ (*Cmcm*) in comparison with (b) $Li_{1-\gamma}CoPO_4$ (*Cmcm*, data reproduced from ref. 21)[a,b]

Sample	(a) $Li_{0.5-\delta}CoPO_4$	(b) $Li_{1-\gamma}CoPO_4$
C (wt%)	0.4(3)	0.8(3)
H (wt%)	0.5(3)	0.4(3)
Li (wt%)	2.0(2)	4.1(2)
Co (wt%)	35(1)	34(1)
P (wt%)	20.0(3)	19.6(3)
n(Li) : *n*(P)	0.45(5)	0.93(5)
n(Co) : *n*(P)	0.93(3)	0.91(3)
Empirical formula	$Li_{0.45(5)}Co_{0.93(3)}P_{1.00(2)}O_4$	$Li_{0.93(5)}Co_{0.91(3)}P_{1.00(2)}O_4$

[a] The molar composition is calculated from the experimental values and normalized to the P content (standard deviations in parentheses). [b] The N and S contents were below the detection limit in both samples (= 0).

As shown in our previous work[21] on *Cmcm*-type $LiCoPO_4$, the synthesis method strongly affects the phase composition. Whereas it was observed that the composition (and also the morphology) can be slightly varied by changing the synthesis technique (solvothermal *vs.* polyol), the molar ratio of the Li, Co, and P precursors represents another, more effective approach towards compositional tuning. For the synthesis of $Li_{1-\gamma}CoPO_4$, the Li : Co : P molar ratio of the starting materials used was 3 : 1 : 10, whereas $Li_{0.5-\delta}CoPO_4$ was obtained from a Li : Co : P ratio of 1 : 1 : 10 (*cf.* experimental part). As a result, different amounts of Li are incorporated in the crystal structures of the products, although the molar amounts of the precursors and contents found in the obtained materials are not correlated linearly. Adjusting the molar ratio of the precursors might therefore provide a synthetic strategy towards other lithium cobalt or transition metal phosphate materials with modified Li contents. Given the fact that the delithiated *Pnma* phases $Li_{2/3}CoPO_4$ and $CoPO_4$ are only accessible by chemical or electrochemical Li extraction from the fully lithiated olivine-type $LiCoPO_4$ (*Pnma*) material[9,13] and also very instable, this bottom-up approach might also pave the way towards the direct and simple soft-chemical preparation of these Li-deficient intermediates. In that matter, the influence of the synthesis route on the chemical composition will have to be thoroughly examined in further experiments.

X-ray absorption spectroscopy

$L_{2,3}$-edge X-ray absorption spectroscopy is highly sensitive to the oxidation state as well as the spin state and chemical environment of transition metals.[28,29] We have therefore applied Co $L_{2,3}$-edge XAS to investigate the chemical state (valency and symmetry) of the cobalt ions in $Li_{0.5-\delta}CoPO_4$ (*Cmcm*) and $Li_{1-\gamma}CoPO_4$ (*Cmcm*). Fig. 3 displays the normalized TEY spectra over the L_3-edge region from this study along with reference

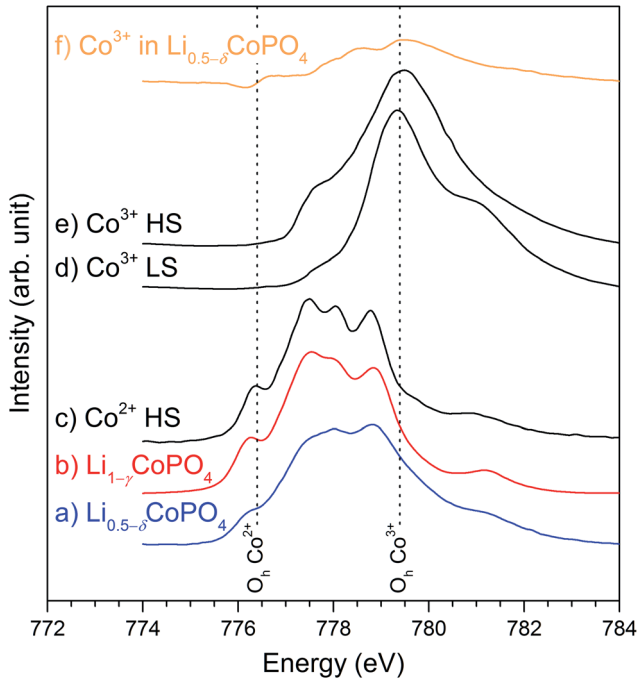

Fig. 3 Normalized Co L_3-edge XAS spectra in the TEY mode for (a) $Li_{0.5-\delta}CoPO_4$ (*Cmcm*, blue), (b) $Li_{1-\gamma}CoPO_4$ (*Cmcm*, red) along with reference spectra for (c) O_h high-spin Co^{2+} in CoO (adapted from ref. 24, black), and (d) low- and (e) high-spin Co^{3+} in $EuCoO_3$ and Sr_2CoO_3Cl (from ref. 30, both black). (f) shows the difference spectrum resulting from a subtraction of 71% Co^{2+} from $Li_{0.5-\delta}CoPO_4$ (orange, $Li_{1-\gamma}CoPO_4$ subtraction), representing the trivalent Co^{3+} ion in the compound. The Co^{3+} association and the lower energy shoulder spectral weight are apparent (see text). All datasets have been aligned to match the common energy scale of ref. 24. The vertical dashed lines indicate the energies corresponding to O_h Co^{2+} (776.4 eV) and O_h Co^{3+} (779.4 eV).

spectra (adapted from (ref. 24 and 30)) for octahedral (O_h) high-spin (HS) Co^{2+} as well as both low-spin (LS) and high-spin (HS) Co^{3+}. $Li_{1-\gamma}CoPO_4$ exhibits all characteristic features of octahedrally (O_h) coordinated Co^{2+}, including the low-energy peak at 776.4 eV that is uniquely ascribed to O_h Co^{2+}.[24,29] Furthermore, overall sharp features can be observed, which indicate a low degree of covalency and energetic alignment with an average octahedral crystal field strength in the order of 1 eV.[29] In fact, a broadening of the CoO spectrum results in a near identical spectrum to $Li_{1-\gamma}CoPO_4$, indicating high purity Co^{2+}, with local disorder being the main difference.

Charge balance arguments suggest that $Li_{0.5-\delta}CoPO_4$ (*Cmcm*) bears cobalt ions in nominal oxidation states of both +2 and +3. Fitting of the spectrum using principal Co^{2+} and Co^{3+} components results in relative contributions of approximately (71 ± 3)% Co^{2+} and (29 ± 3)% Co^{3+} (as opposed to (97 ± 3)% Co^{2+} and (3 ± 3)% Co^{3+} for $Li_{1-\gamma}CoPO_4$), where the symmetry and spin state of the trivalent Co has some, but not dominating effects on the distribution. These values are in line with the Co^{2+} and Co^{3+} contents expected on basis of the nominal composition $Li_{0.5-\delta}CoPO_4$ (~50% Co^{2+} and ~50% Co^{3+}), but where the Co^{3+} contribution derived from XAS is lower. The discrepancy can partly be explained by a small but noticeable reduction at the surface, in line with the fact that Co^{3+} is significantly less stable than Co^{2+}. Moreover, the material was produced using a TTEG solvent, which also acts as a weak reducing agent[31,32] and hence, might reduce the Co^{3+} concentration on the particle surface (*cf.* probing depth of TEY: 2–5 nm). We note that the more bulk sensitive spectra (FY, not shown) indicated higher spectral weight towards higher energies (and thus more Co^{3+} in the bulk), consistent with this hypothesis, but the spectra are not of high enough quality to be analyzed or discussed further.

In order to learn more about the symmetry and spin of the Co^{3+} sites, we have subtracted the fitted Co^{2+} contribution from the $Li_{0.5-\delta}CoPO_4$ spectrum (Fig. 3f). We note that while the main intensity difference is centered around the energy associated with the main peak of Co^{3+} (779.4 V), there is significant intensity on the low-energy side of this peak that is not accounted for by the LS Co^{3+}. Comparison with Co^{3+} ref. 30 of different spin indicates that the trivalent Co ions are primarily high-spin, which can be rationalized based on the tetragonal distortions in the [CoO_6] octahedra (*cf.* Table S3, ESI†) and the analogous HS Co^{3+} *L*-edge spectral assignment upon axial elongations and equatorial contractions in various perovskites[30,33,34]. The XAS thus indicates that the Li vacancies are indeed inducing distortions near the Co^{3+} sites that favor the HS Co^{3+} state. The HS Co^{3+} state is also consistent with a larger average Co–O distance (*i.e.*, larger ionic radius) than what would be expected from the (smaller) LS Co^{3+} that only occupies the t_{2g} orbitals and is associated with a stronger, more covalent Co–O interaction (*cf.* Table S3, ESI†). The presence of HS Co^{3+} is further consistent with the large magnetic moment (see later).

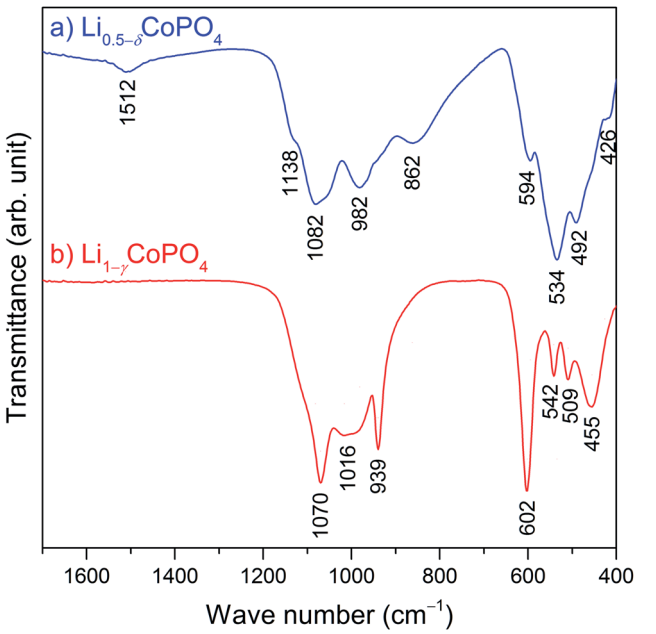

Fig. 4 Comparison of the FTIR spectra of (a) $Li_{0.5-\delta}CoPO_4$ (*Cmcm*, blue), and (b) $Li_{1-\gamma}CoPO_4$ (*Cmcm*, red, data reproduced from ref. 21). The omitted region of 1700–4000 cm^{-1} (*cf.* Fig. S6, ESI†) does not show any absorption bands of water or other impurities.

Infrared spectroscopy

Fig. 4 compares the infrared spectra of $Li_{0.5-\delta}CoPO_4$ (*Cmcm*) and $Li_{1-\gamma}CoPO_4$ (*Cmcm*; data reproduced from ref. 21) in the range of 400–1700 cm^{-1}. The omitted region from 1700 cm^{-1} to 4000 cm^{-1} is presented in Fig. S6 (ESI†) and does not show any absorption bands of water or other impurities. As expected, both spectra are dominated by the four fundamental vibrations of the pseudo-tetrahedral phosphate groups. Two regions can be distinguished, with the symmetric (ν_1) and asymmetric (ν_3) stretching vibrations of P–O being observed at higher frequencies, as well as the symmetric (ν_2) and asymmetric (ν_4) bending vibrations of the O–P–O group at lower frequencies. According to previous reports,[16,21] the absorption peaks of *Cmcm*-type $Li_{1-\gamma}CoPO_4$ (Fig. 4b) can be assigned as follows: the ν_1 and ν_3 stretching modes are observed at 1070 cm^{-1}, 1016 cm^{-1}, and 939 cm^{-1}, whereas the ν_2 and ν_4 deformation vibrations appear in the region of 455–602 cm^{-1}. Despite the structural similarity of the compounds, the IR spectrum of $Li_{0.5-\delta}CoPO_4$ (*Cmcm*, Fig. 4a) shows some distinct differences, in particular a shift of the band frequencies to slightly lower energies and band broadening, and the appearance of additional weak bands at 1512 cm^{-1} and 1138 cm^{-1}.

The changes observed for the Li-deficient phase $Li_{0.5-\delta}CoPO_4$ are in line with reports[35,36] on olivine-type Li_xFePO_4 ($0 \leq x \leq 1$) which demonstrated that the absorption modes of the $[PO_4]^{3-}$ groups are extremely sensitive to the delithiation of $LiFePO_4$ and the associated oxidation of Fe^{2+} to Fe^{3+}. As discussed, the average P–O distances in $Li_{1-\gamma}CoPO_4$ (*Cmcm*) remain virtually unchanged when less Li is incorporated in the structure (*cf.* Table S3, ESI†). Hence, the energies of the absorption modes are not changed drastically, indicating similar local structures of the $[PO_4]^{3-}$ units. This is in good agreement with a report by Popović and co-workers,[37] which suggested a linear correlation between the P–O bond lengths and stretching frequencies. The observed band splitting, on the other hand, is correlated with interactions between ions, in this case between the $[PO_4]^{3-}$ units and the adjacent Li^+ and $Co^{2+/3+}$ cations, *i.e.* the stronger the interaction, the larger the factor group splitting effects.[36] In fact, the P–Li and P–Co distances are reduced in $Li_{0.5-\delta}CoPO_4$ compared to $Li_{1-\gamma}CoPO_4$ (Table S3, ESI†), which leads to stronger interactions. Furthermore, it was shown[38,39] that the factor group splitting of the ν_3 modes increases with the second ionization potential of the transition metal due to the formation of strong bonds with the oxygen atoms of the $[PO_4]$ units, which causes a redistribution of electron density in the P–O bonds. This is reflected in the observation that the P–O1 bonds are expanded, and the P–O2 bonds shortened by ~0.02 Å each in $Li_{0.5-\delta}CoPO_4$ (*cf.* Table S3, ESI†). Due to the significantly higher ionization potential of Co^{3+} compared to Co^{2+}, the larger factor group splitting in the IR spectrum of $Li_{0.5-\delta}CoPO_4$ is therefore the result of the mixed valence state of the Co ions in the structure (Co^{2+}/Co^{3+}) as opposed to $Li_{1-\gamma}CoPO_4$ which contains Co^{2+} only. However, a thorough analysis of the spectra, including the assignment of the additional absorption band at 1512 cm^{-1}, would require a complete structural model, including the ordering of the Li^+, Co^{2+}, and Co^{3+} ions in the framework as well as DFT calculations, which is beyond the scope of this work. It is likely that the occurrence of additional modes is the result of a lower local symmetry in $Li_{0.5-\delta}CoPO_4$ due to a higher defect concentration.

Magnetic properties

Fig. 5 shows the magnetic susceptibility as function of temperature measured at a magnetic field of 0.1 T in field-cooled (FC) condition as well as the magnetic hysteresis recorded at a temperature of 2 K of $Li_{0.5-\delta}CoPO_4$ in comparison with $Li_{1-\gamma}CoPO_4$ (both *Cmcm*). The temperature dependence of the magnetic susceptibilities indicates a long-range antiferromagnetic to paramagnetic transition at T_N = 10.5 K for $Li_{0.5-\delta}CoPO_4$, and T_N = 12 K for $Li_{1-\gamma}CoPO_4$, respectively. The low transition temperature T_N of 12 K of the $Li_{1-\gamma}CoPO_4$ (*Cmcm*) phase is in agreement with our previous study[21] on *Cmcm*-type $LiCoPO_4$ and is comparable to the non-olivine, metastable $LiCoPO_4$ ($Pna2_1$) phase (T_N = 11 K),[18] but much lower than the well investigated olivine-type $LiCoPO_4$ (*Pnma*, T_N = 21.6 K).[40,41] This finding demonstrates the close relation between structural and magnetic properties. However, the further reduction of the observed transition temperature T_N of the Li-deficient $Li_{0.5-\delta}CoPO_4$ (*Cmcm*) compound might be related to the vacancies on the Co site, weakening the Co–O–Co super exchange interaction. Above the transition temperature, the magnetic susceptibility of both compounds follow the Curie–Weiss law (see Fig. S7, ESI†), $\chi = \chi_0 + (N_A\mu_{eff}^2)/(3k_b(T - \theta_C))$, where χ_0 is a temperature-independent contribution, μ_{eff} the effective magnetic moment, N_A the Avogadro number, θ_C the Weiss temperature, and k_b the Boltzmann constant. Fitting the high-temperature magnetic susceptibility with the Curie–Weiss law yields a higher Weiss temperature of −21.8 K of $Li_{0.5-\delta}CoPO_4$ compared to the stoichiometric $Li_{1-\gamma}CoPO_4$ (−28.2 K; *cf.* inset of Fig. S7, ESI†), which reflects the difference in transition

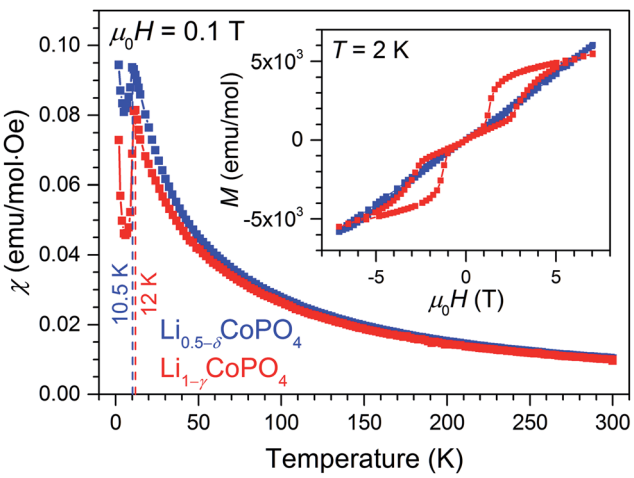

Fig. 5 Magnetic susceptibility as function of temperature of $Li_{0.5-\delta}CoPO_4$ (*Cmcm*, blue data points) and $Li_{1-\gamma}CoPO_4$ (*Cmcm*, red) measured at a magnetic field of 0.1 T in field-cooled condition. The vertical dashed lines mark the respective transition temperatures of both phases (10.5 K and 12 K). The inset shows the corresponding magnetic hysteresis curves recorded at T = 2 K.

temperatures T_N. Furthermore, similar effective magnetic moments of $\mu_{eff} = (5.20 \pm 0.02)\ \mu_B$ for $Li_{0.5-\delta}CoPO_4$ and $(5.08 \pm 0.02)\ \mu_B$ for $Li_{1-\gamma}CoPO_4$ were found. Both values exceed the spin-only value of high-spin Co^{2+} and Co^{3+} (3.9 μ_B and 4.8 μ_B, respectively), demonstrating a non-negligible orbital contribution.[42] Taking into account the finite angular momentum, effective magnetic moments of 5.2 μ_B and 5.5 μ_B for high-spin Co^{2+} and Co^{3+} in the O_h symmetry ($^5t_{2g}$ and $^4t_{1g}$ ground state) are expected in the weak spin–orbit coupling limit. Assuming the presence of only Co^{2+} in the $Li_{1-\gamma}CoPO_4$ compound, the observed values are slightly smaller than the expected ones. However, the larger effective magnetic moment μ_{eff} of $Li_{0.5-\delta}CoPO_4$ clearly supports the findings of a mixed valence state of Co in the Li-deficient compound as discussed in the previous sections.

The inset of Fig. 5 reveals a more distinct difference of the magnetic properties of $Li_{1-\gamma}CoPO_4$ and the Li-deficient $Li_{0.5-\delta}CoPO_4$ compounds. $LiCoPO_4$ exhibits a magnetic double-hysteresis loop at 2 K, demonstrating an antiferromagnetic ground state at 0 T (for the hysteresis curves at 11 K and 300 K see Fig. S8, ESI†). Furthermore, the double-hysteresis loop indicates a spin-flip transition at a critical field of around ±3 T, which is much lower than for *Pnma*-type $LiCoPO_4$.[43] Again, this can be attributed to the different structural properties. In contrast, an almost linear dependence of the magnetization as a function of the applied field is observed for $Li_{0.5-\delta}CoPO_4$ below T_N. No hysteresis with a finite remanence caused by a weak ferromagnetic phase due to the mixed-valence state of Co ions were found.[40] However, the difference of the magnetic susceptibility recorded under field-cooled (FC) and zero field-cooled (ZFC) conditions suggests the formation of magnetic domains below $T \approx 5$ K. Below this temperature, the finite amount of Co^{3+} ions as well as the observed defects on the Co sites might cause competing magnetic interactions resulting in a complex antiferromagnetic state as, for instance, described by Jensen and co-workers.[44]

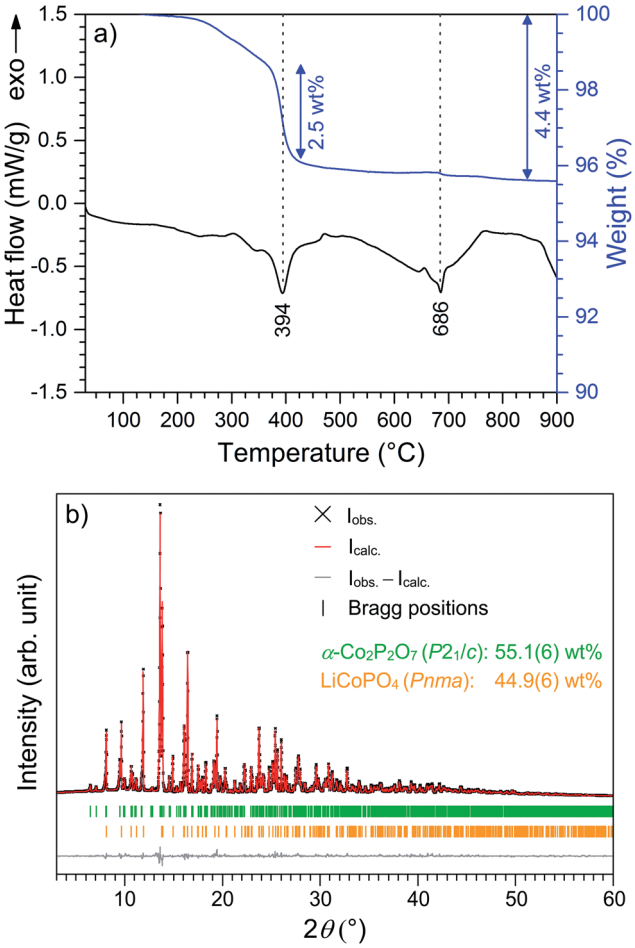

Fig. 6 (a) DSC (black) and TGA (blue) curves of $Li_{0.5-\delta}CoPO_4$ (*Cmcm*) measured in a temperature range of 30–900 °C (heating rate: 10 °C min^{-1}, atmosphere: synthetic air). Two endothermic DSC signals are observed at 394 °C (accompanied by a TGA weight loss step of ~2.5 wt%) and 686 °C, respectively. (b) Rietveld fit of the X-ray powder diffraction data (transmission geometry, Mo $K_{\alpha 1}$ radiation) of the dark violet post TGA/DSC-material demonstrating that mixture of olivine-type $LiCoPO_4$ (*Pnma*) and α-$Co_2P_2O_7$ ($P2_1/c$) was formed upon heating.

Thermal stability

The thermal stability of $Li_{0.5-\delta}CoPO_4$ (*Cmcm*) was investigated using TGA/DSC (Fig. 6) and temperature-dependent *in situ* X-ray powder diffraction, both performed under air (Fig. 7). The thermal behavior of $LiCoPO_4$ (*Cmcm*) has been discussed in detail in ref. 21. In the TGA curve (Fig. 6a), an overall mass loss of ~4.8 wt% is observed between 30 °C and 900 °C, which proceeds in several steps. The mass loss of ~1.3 wt% up to 360 °C is probably correlated with the decomposition of residues of the TTEG solvent and the acetate precursors (*cf.* CHNS analysis, Table 2). The DSC curve shows two pronounced, broad endothermic peaks at 394 °C and 686 °C, respectively, with the first signal being accompanied by a weight loss step of ~2.5 wt% and the second one of ~0.1 wt%. The corresponding X-ray powder diffraction pattern (Fig. 6b, refinement details see Tables S7–S11†) of the dark violet powder (*cf.* graphical abstract) obtained after the TGA/DSC measurement reveals that a mixture of 44.9(6) wt% olivine-type $LiCoPO_4$ (*Pnma*, ICSD no. 431999)[45] and 55.1(6) wt% of the low-temperature modification of cobalt pyrophosphate, α-$Co_2P_2O_7$ ($P2_1/c$, ICSD no. 280959)[46] was formed. Note that data obtained from a similar experiment using an argon atmosphere are in good agreement (Fig. S9 and S10, Tables S12–S16, ESI†).

In order to understand the signals observed in the TGA/DSC study and to identify possible intermediates of the heating process, we performed a temperature-controlled *in situ* PXRD experiment between room temperature (30 °C) and 900 °C with a step size of 100 °C (Fig. 7). The Rietveld fits of the individual PXRD patterns at each temperature up to 700 °C can be found in Fig. S11 (ESI†). The refined phase fractions and crystallographic details (atomic coordinates, thermal displacements parameters, bond lengths), reflecting the structural changes, are presented in Tables S17–S25.† (Note that the patterns at $T \geq 800$ °C, which are shown in Fig. S12 (ESI†), were of insufficient quality for a refinement because of the occurrence of strong reflections from the corundum sample holder.) Up to 300 °C, no change of

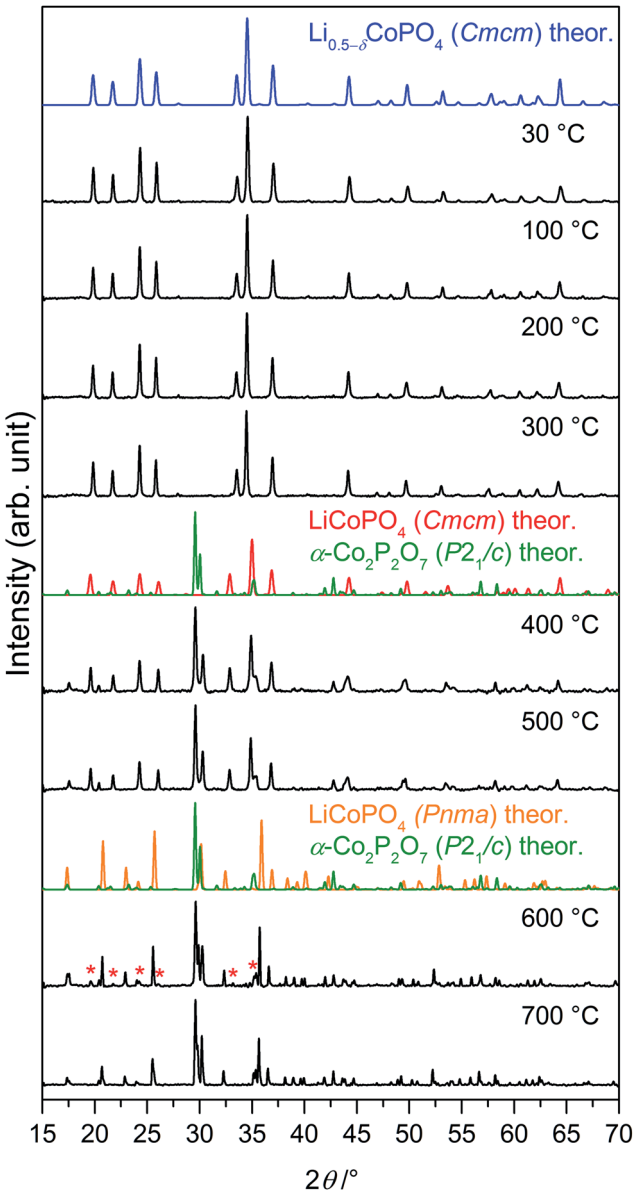

Fig. 7 *In situ* X-ray powder diffraction patterns (Bragg–Brentano geometry, Cu K_α radiation) of $Li_{0.5-\delta}CoPO_4$ (*Cmcm*) measured between 30 °C and 700 °C under air (heating rate: 5 °C min^{-1}; for patterns at 800 °C, 900 °C, and after cooling see Fig. S12, ESI†). The phase undergoes several transitions upon heating. The theoretical patterns of the involved phases, which were calculated from room temperature data, are displayed in color. Between 300 °C and 400 °C, $Li_{0.5-\delta}CoPO_4$ (*Cmcm*, this work, blue) decomposes to $LiCoPO_4$ (*Cmcm*, ICSD no. 432186,[21] red) and α-$Co_2P_2O_7$ ($P2_1/c$, ICSD no. 280959,[46] green). Above 500 °C, an irreversible transition of $LiCoPO_4$ (*Cmcm*, blue) to olivine-type $LiCoPO_4$ (*Pnma*, ICSD no. 431999,[45] orange) occurs. The reflections marked with red asterisks (*) in the pattern at 600 °C can be assigned to residues of $LiCoPO_4$ (*Cmcm*).

the diffraction patterns occurs, indicating that the $Li_{0.5-\delta}CoPO_4$ (*Cmcm*) phase is thermally stable up to that temperature. Between 300 °C and 400 °C, a mixture of the 'fully lithiated' $Li_{1-\gamma}CoPO_4$ (*Cmcm*) structure (referred to as $LiCoPO_4$ with $\gamma = 0$ in Fig. 7 since ICSD no. 432186 (ref. 21) was used for the theoretical pattern) and α-$Co_2P_2O_7$ ($P2_1/c$) is observed. Hence, the endothermic DSC signal at 395 °C can be explained by the decomposition of $Li_{0.5-\delta}CoPO_4$ (*Cmcm*) to these phases (the simultaneous mass loss will be explained later in the text). Between 500 °C and 600 °C, the *Cmcm*-type $Li_{1-\gamma}CoPO_4$ intermediate starts to convert to the thermodynamically more stable olivine *Pnma* structure, whereas the peaks of α-$Co_2P_2O_7$ remain unaltered. The fact that the low-temperature α-modification of $Co_2P_2O_7$ ($P2_1/c$) does not transform to the high-temperature β-$Co_2P_2O_7$ ($A2/m$)[47] phase, which would be expected at ~480 °C (ref. 48) for the pure material, suggests that the transformation is either kinetically hindered or very slow. Hence, the DSC signal at 688 °C corresponds to the transformation of the *Cmcm* to the *Pnma* $LiCoPO_4$ phase. The lower transition temperature found in the *in situ* PXRD study compared to the DSC data might be related to slightly different atmospheres (air *vs.* synthetic air) and heating rates (10 °C min^{-1} *vs.* 5 °C min^{-1}) being used. The phase transformation is not completed until 700 °C because traces of $Li_{1-\gamma}CoPO_4$ (*Cmcm*) can be identified in the diffraction pattern at 600 °C. Compared to the thermal stability of the pure, lithiated $LiCoPO_4$ (*Cmcm*) material (transformation to single-phase $LiCoPO_4$ (*Pnma*) at 575 °C),[21] the phase transition temperature is significantly increased. No further phase changes are observed in the PXRD patterns up to 700 °C, yet the diffraction peaks are shifted to lower angles, indicating bigger lattice dimensions due to thermal expansion. Unfortunately, it cannot be derived from the patterns at $T \geq 800$ °C (see Fig. S12, ESI†) whether the $Pna2_1$-type $LiCoPO_4$ structure reappears as a high-temperature phase as reported for all three, fully lithiated $LiCoPO_4$ polymorphs (*Pnma*,[17] $Pna2_1$,[19] and *Cmcm*[21]). The pattern of the cooled sample (25 °C; Fig. S12, ESI†) is consistent with the *ex situ* PXRD experiment (Fig. 6b) and shows reflections of α-$Co_2P_2O_7$ and *Pnma*-type $LiCoPO_4$, indicating that both phase transitions are irreversible.

The results of the thorough investigation of the thermal stability of the Li-deficient compound $Li_{0.5-\delta}CoPO_4$ demonstrate that the phase exhibits a complex behavior upon heating which involves several phase transitions. Based on the combined approach using TGA, DSC (Fig. 6), and *in situ* PXRD studies (Fig. 7), a decomposition mechanism can be proposed according to Scheme 1. Note that since it is not possible to determine the composition of the decomposition products and intermediates (which are likely to be deficient in Li and Co as well), the mechanism is presented on basis of the nominal composition $Li_{0.5-\delta}CoPO_4$ with $\delta = 0$. In the first step (eqn (I)), $LiCoPO_4$ (*Cmcm*) and $Co_2P_2O_7$ ($P2_1/c$; both with Co oxidation state +2) are formed from four equivalents of the Co^{2+}/Co^{3+} mixed-valent starting material $Li_{0.5-\delta}CoPO_4$ (*Cmcm*). This step is based on a redox reaction, in which the two Co^{3+} equivalents from the four $Li_{0.5-\delta}CoPO_4$ ($\delta = 0$) units are reduced by O^{2-} ions (eqn (Ia)), which are released upon the pyrophosphate formation (*i.e.*, coupling of isolated $[PO_4]$ tetrahedra to $[P_2O_7]$ units *via* shared corners). The O^{2-} ions are in turn oxidized to form elemental oxygen (eqn (Ib)) that is released. The O_2 release from the phosphate groups corresponds to an approximate mass loss of ~2.5 wt% which in full agreement with the TGA mass loss step observed at 394 °C (*cf.* Fig. 6a). The estimated mass fractions of $Li_{1-\gamma}CoPO_4$ (*Cmcm*, with $\gamma = 0$) and $Co_2P_2O_7$ after the

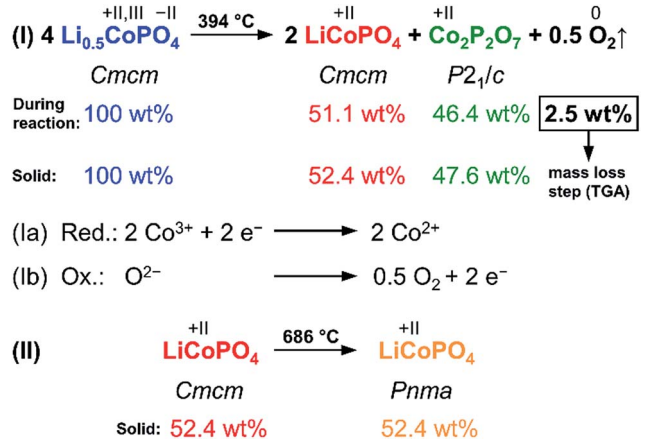

Scheme 1 Proposed two-step mechanism of the thermal decomposition of $Li_{0.5-\delta}CoPO_4$ (*Cmcm*, with $\delta = 0$) and theoretically expected weight fractions (in wt%) of the involved phases during the reaction as well as in the solid remainder after O_2 release. It can be inferred that the TGA weight loss (*cf.* Fig. 7) at 394 °C is due to the release of oxygen as a result of a redox process. The color code of the phases is related to Fig. 6 and 7.

oxygen release are ~52.4 wt% and ~47.6 wt%, respectively, and are very close to the refined values obtained from our Rietveld analysis (*cf.* Fig. 6, and Table S17, ESI†). The slight deviation of our refined values from the calculated ones can be explained by the fact that the nominal composition was used for this hypothesis and that the refinement of phase fractions on basis of the reflection intensities depends on the particle size and crystallinity. In the second step at 686 °C (eqn (II)), which was not accompanied by a significant mass loss in the TGA (Fig. 6a), $LiCoPO_4$ (*Cmcm*) is transformed to the thermodynamically more stable olivine-type $LiCoPO_4$ (*Pnma*) as observed in the PXRD study (Fig. 6b).

Interestingly, the decomposition leads to the crystallization of same phases (*Pnma*-type $LiCoPO_4$ and $Co_2P_2O_7$) under oxygen evolution as reported for the olivine-like Li-poor phase Li_xCoPO_4.[13] However, there are some significant mechanistic differences between $Li_{0.5-\delta}CoPO_4$ (*Cmcm*) and Li_xCoPO_4 (*Pnma*), which might be due to the fact that our studies are based on the pristine material whereas the studies on Li_xCoPO_4 were based on charged $LiCoPO_4$ electrodes. First of all, as reported by Bramnik *et al.*,[13] the decomposition of Li_xCoPO_4 cathodes occurs at much lower temperatures (<200 °C) suggesting that the Li-poor, *Cmcm*-type $Li_{0.5-\delta}CoPO_4$ phase (decomposition at 394 °C) is significantly more stable. (Note that compared to the results of Theil *et al.*,[14] on the other hand, *Cmcm*-type $Li_{0.5-\delta}CoPO_4$ seems to be less stable than Li_xCoPO_4, which was found to be thermally stable at least up to 550 °C. This discrepancy might be explained by different particle sizes and carbon contents.). Furthermore, in contrast to our material, the $Co_2P_2O_7$ crystallization was found to be not proceeding simultaneously, but at higher temperature than the Li_xCoPO_4 (*Pnma*) decomposition, which was related to a possibly amorphous intermediate.[13] In addition, the decomposition process was suggested to be promoted by carbon present in samples, which reacts with the released oxygen to form CO_2 gas.[13] The crucial influence/destabilizing effect of carbon on the thermal stability was also confirmed for charged $LiCoPO_4$ electrodes containing $CoPO_4$.[14] Based on this work, however, there is no indication that carbon affects the decomposition of the pristine $Li_{0.5-\delta}CoPO_4$ (*Cmcm*) material since the carbon content of our material is not significant (0.4(3) wt%, *cf.* Table 2). To clarify whether this is also the case for the pristine, carbon-free Li_xCoPO_4 ($x = 0$, 0.7; space group *Pnma*) olivine phases (as opposed to the studies[13,14] based on carbon-containing charged $LiCoPO_4$ electrodes), our direct synthetic approach might provide a pathway to get a deeper understanding of their intrinsic thermal stabilities as well.

Conclusions

In this study, a polyol synthesis pathway towards the first Li-deficient structural derivative of the *Cmcm* polymorph of $LiCoPO_4$ with the nominal composition $Li_{0.5-\delta}CoPO_4$ and its material properties were presented. To the best of our knowledge, this is also the first time that a sub-stoichiometric Li_xCoPO_4 phase was synthesized using a soft-chemical bottom-up approach as opposed to common chemical and electrochemical Li extraction techniques starting from $LiCoPO_4$-type materials.

Neutron and X-ray powder diffraction experiments as well as elemental analysis suggested that $Li_{0.5-\delta}CoPO_4$ (*Cmcm*) is non-stoichiometric and deficient both in Li and Co, which generates vacancies on both cation sub-lattices in the crystal structure. The occurrence of vacancies was also observed in the course of a structure redetermination of the 'fully lithiated' *Cmcm* phase, resulting in the revised formula $Li_{1-\gamma}CoPO_4$. Co $L_{2,3}$-edge X-ray absorption spectroscopy indicated that, unlike $Li_{1-\gamma}CoPO_4$ which exclusively contains octahedrally coordinated Co^{2+} ions, the Li-deficient structure bears both Co^{2+} and Co^{3+} ions to compensate for the Li deficit. Due to the reduced Li content and amount of electrochemically active Co^{2+} ions, the material exhibited a poor electrochemical performance. The thermal stability of $Li_{0.5-\delta}CoPO_4$ has been studied thoroughly using thermogravimetry, differential scanning calorimetry, and temperature-dependent *in situ* X-ray powder diffraction experiments. $Li_{0.5-\delta}CoPO_4$ (*Cmcm*) is metastable and shows a complex, two-step decomposition mechanism upon heating. At 394 °C, it decomposes to α-$Co_2P_2O_7$ ($P2_1/c$) and $Li_{1-\gamma}CoPO_4$ (*Cmcm*) in an endothermic reaction upon which oxygen is released as a result of a redox reaction. The $Li_{1-\gamma}CoPO_4$ (*Cmcm*) phase then irreversibly converts to the thermodynamically more stable $LiCoPO_4$ (*Pnma*) olivine structure at 686 °C.

To conclude, the present work paves the way towards the direct and simple soft-chemical preparation and investigation of Li-deficient structures derived from lithium transition-metal phosphates. Our methodology provides fundamental insights into the material properties, and hence to study Li-deficient intermediates that are probably involved in the charge/discharge steps of $LiCoPO_4$-type cathodes. It further helps to understand the complex structure chemistry of this class of cathode materials for Li-ion batteries. In that matter, future studies should focus on compositional tuning (*e.g.* by

modifying the amounts of the precursors in the synthesis) in order to identify other partially lithiated structural derivatives.

Author contributions

J. L. performed the material characterization using *in situ* and *ex situ* PXRD, SEM/EDS, IR spectroscopy, and electrochemical measurements, and analyzed the data (under supervision of T. N. and M. M. D.). C. A.-S. performed the synthesis. S. G. and D. N. performed and analyzed magnetic and XAS measurements, respectively. I. P. O. and C. A.-S. conducted neutron diffraction experiments. J. L. wrote the manuscript. All authors have given approval to the final version of the manuscript.

Funding sources

This work has been funded by the Fonds der Chemischen Industrie and the TUM Graduate School. The use of the Stanford Synchrotron Radiation Lightsource (SSRL), SLAC National Accelerator Laboratory, is supported by the US Department of Energy, Office of Science, and Office of Basic Energy Sciences (contract no. DE-AC02-76SF00515). We further thank the Institut Laue-Langevin (ILL) for beam time allocation, and the D2B team for technical support (proposal no. 5-31-2531).

Abbreviations

AAS	Atomic absorption spectroscopy
AEY	Auger electron yield
DFT	Density functional theory
DSC	Differential scanning calorimetry
EDS	Energy-dispersive X-ray spectroscopy
FC	Field-cooled
FTIR	Fourier-transform infrared
FY	Fluorescence yield
HS	High-spin
ICSD	Inorganic Crystal Structure Database
LS	Low-spin
NPD	Neutron powder diffraction
PXRD	Powder X-ray diffraction
SEM	Scanning electron microscope
SQUID	Superconducting quantum interference device
TEY	Total electron yield
TGA	Thermogravimetric analysis
TTEG	Tetraethylene glycol
XAS	X-ray absorption spectroscopy
ZFC	Zero field-cooled

Acknowledgements

The authors thank U. Ammari for elemental analysis, and D. Haering for TGA/DSC measurements. J. L. and C. A.-S. are grateful to the TUM Graduate School, the Fonds der Chemischen Industrie, DAAD and Colciencias for financial support of their Ph.D. work.

References

1 K. Amine, H. Yasuda and M. Yamachi, *Electrochem. Solid-State Lett.*, 2000, **3**, 178–179.
2 J. M. Tarascon and M. Armand, *Nature*, 2001, **414**, 359–367.
3 B. L. Ellis, K. T. Lee and L. F. Nazar, *Chem. Mater.*, 2010, **22**, 691–714.
4 K. Zaghib, A. Guerfi, P. Hovington, A. Vijh, M. Trudeau, A. Mauger, J. B. Goodenough and C. M. Julien, *J. Power Sources*, 2013, **232**, 357–369.
5 A. Yamada, M. Hosoya, S.-C. Chung, Y. Kudo, K. Hinokuma, K.-Y. Liu and Y. Nishi, *J. Power Sources*, 2003, **119–121**, 232–238.
6 S. Okada, S. Sawa, M. Egashira, J. Yamaki, M. Tabuchi, H. Kageyama, T. Konishi and A. Yoshino, *J. Power Sources*, 2001, **97–98**, 430–432.
7 B. Kang and G. Ceder, *Nature*, 2009, **458**, 190–193.
8 N. N. Bramnik, K. Nikolowski, C. Baehtz, K. G. Bramnik and H. Ehrenberg, *Chem. Mater.*, 2007, **19**, 908–915.
9 H. Ehrenberg, N. N. Bramnik, A. Senyshyn and H. Fuess, *Solid State Sci.*, 2009, **11**, 18–23.
10 H. Ju, J. Wu and Y. Xu, *Int. J. Energy Environ. Eng.*, 2013, **4**(22), 26.
11 M. Kaus, I. Issac, R. Heinzmann, S. Doyle, S. Mangold, H. Hahn, V. S. K. Chakravadhanula, C. Kuebel, H. Ehrenberg and S. Indris, *J. Phys. Chem. C*, 2014, **118**, 17279–17290.
12 F. C. Strobridge, R. J. Clement, M. Leskes, D. S. Middlemiss, O. J. Borkiewicz, K. M. Wiaderek, K. W. Chapman, P. J. Chupas and C. P. Grey, *Chem. Mater.*, 2014, **26**, 6193–6205.
13 N. N. Bramnik, K. Nikolowski, D. M. Trots and H. Ehrenberg, *Electrochem. Solid-State Lett.*, 2008, **11**, A89–A93.
14 S. Theil, M. Fleischhammer, P. Axmann and M. Wohlfahrt-Mehrens, *J. Power Sources*, 2013, **222**, 72–78.
15 X. Huang, J. Ma, P. Wu, Y. Hu, J. Dai, Z. Zhu, H. Chen and H. Wang, *Mater. Lett.*, 2005, **59**, 578–582.
16 K. J. Kreder, G. Assat and A. Manthiram, *Chem. Mater.*, 2015, **27**, 5543–5549.
17 J. Ludwig, C. Marino, D. Haering, C. Stinner, D. Nordlund, M. M. Doeff, H. A. Gasteiger and T. Nilges, *RSC Adv.*, 2016, **6**, 82984–82994.
18 C. Jaehne, C. Neef, C. Koo, H.-P. Meyer and R. Klingeler, *J. Mater. Chem. A*, 2013, **1**, 2856–2862.
19 J. Ludwig, D. Nordlund, M. M. Doeff and T. Nilges, *J. Solid State Chem.*, 2017, **248**, 9–17.
20 U. Amador, J. M. Gallardo-Amores, G. Heymann, H. Huppertz, E. Moran and M. E. Arroyo-de Dompablo, *Solid State Sci.*, 2009, **11**, 343–348.
21 C. Alarcón-Suesca, J. Ludwig, V. Hlukhyy, C. Stinner and T. Nilges, *Inorganics*, 2016, **4**, 35.
22 V. Petricek, M. Dusek and L. Palatinus, *Z. Kristallogr.–Cryst. Mater.*, 2014, **229**, 345–352.
23 J. Rodriguez-Carvajal, *Phys. B*, 1993, **192**, 55–69.
24 A. M. Hibberd, H. Q. Doan, E. N. Glass, F. M. F. de Groot, C. L. Hill and T. Cuk, *J. Phys. Chem. C*, 2015, **119**, 4173–4179.

25 D. T. Cromer and D. A. Liberman, *Acta Crystallogr., Sect. A: Cryst. Phys., Diffr., Theor. Gen. Crystallogr.*, 1981, **37**, 267–268.
26 J. Chen and M. S. Whittingham, *Electrochem. Commun.*, 2006, **8**, 855–858.
27 O. Garcia-Moreno, M. Alvarez-Vega, F. Garcia-Alvarado, J. Garcia-Jaca, J. M. Gallardo-Amores, M. L. Sanjuan and U. Amador, *Chem. Mater.*, 2001, **13**, 1570–1576.
28 F. M. F. de Groot, J. C. Fuggle, B. T. Thole and G. A. Sawatzky, *Phys. Rev. B: Condens. Matter*, 1990, **42**, 5459–5468.
29 F. M. F. de Groot, M. Abbate, J. van Elp, G. A. Sawatzky, Y. J. Ma, C. T. Chen and F. Sette, *J. Phys.: Condens. Matter*, 1993, **5**, 2277–2288.
30 Z. Hu, H. Wu, M. W. Haverkort, H. H. Hsieh, H. J. Lin, T. Lorenz, J. Baier, A. Reichl, I. Bonn, C. Felser, A. Tanaka, C. T. Chen and L. H. Tjeng, *Phys. Rev. Lett.*, 2004, **92**, 207402.
31 D.-H. Kim and J. Kim, *Electrochem. Solid-State Lett.*, 2006, **9**, A439–A442.
32 M. K. Devaraju and I. Honma, *Adv. Energy Mater.*, 2012, **2**, 284–297.
33 M. Abbate, J. C. Fuggle, A. Fujimori, L. H. Tjeng, C. T. Chen, R. Potze, G. A. Sawatzky, H. Eisaki and S. Uchida, *Phys. Rev. B: Condens. Matter Mater. Phys.*, 1993, **47**, 16124–16130.
34 S. Y. Istomin, O. A. Tyablikov, S. M. Kazakov, E. V. Antipov, A. I. Kurbakov, A. A. Tsirlin, N. Hollmann, Y. Y. Chin, H. J. Lin, C. T. Chen, A. Tanaka, L. H. Tjeng and Z. Hu, *Dalton Trans.*, 2015, **44**, 10708–10713.
35 C. M. Burba and R. Frech, *J. Electrochem. Soc.*, 2004, **151**, A1032–A1038.
36 C. M. Burba and R. Frech, *Spectrochim. Acta, Part A*, 2006, **65**, 44–50.
37 L. Popović, D. De Waal and J. C. A. Boeyens, *J. Raman Spectrosc.*, 2005, **36**, 2–11.
38 M. T. Paques-Ledent and P. Tarte, *Spectrochim. Acta, Part A*, 1974, **30**, 673–689.
39 A. Ait Salah, P. Jozwiak, J. Garbarczyk, K. Benkhouja, K. Zaghib, F. Gendron and C. M. Julien, *J. Power Sources*, 2005, **140**, 370–375.
40 N. F. Kharchenko, Y. N. Kharchenko, R. Szymczak, M. Baran and H. Schmid, *Low Temp. Phys.*, 2001, **27**, 895–898.
41 J. P. Rivera, *Ferroelectrics*, 1994, **161**, 147–164.
42 S. H. Baek, R. Klingeler, C. Neef, C. Koo, B. Buechner and H. J. Grafe, *Phys. Rev. B: Condens. Matter Mater. Phys.*, 2014, **89**, 134424.
43 N. F. Kharchenko, V. M. Khrustalev and V. N. Savitskii, *Low Temp. Phys.*, 2010, **36**, 558–564.
44 M. H. Jensen and P. Bak, *Phys. Rev. B: Condens. Matter Mater. Phys.*, 1983, **27**, 6853–6868.
45 J. Ludwig, C. Marino, D. Haering, C. Stinner, H. A. Gasteiger and T. Nilges, *J. Power Sources*, 2017, **342**, 214–223.
46 B. El Bali and M. Bolte, *Acta Crystallogr., Sect. E: Struct. Rep. Online*, 2002, **58**, i32–i33.
47 A. El Belghitti, A. Boukhari and E. M. Holt, *Acta Crystallogr., Sect. C: Cryst. Struct. Commun.*, 1994, **50**, 482–484.
48 M. Trojan and D. Brandova, *Sb. Ved. Pr. - Vys. Sk. Chemickotechnol. Pardubice*, 1985, **47**, 33–42.